

The Seasonal Cycle of Significant Wave Height in the Ocean: Local vs Remote Forcing

Luke Colosi¹, Ana B. Villas Bôas¹, Sarah T. Gille¹

¹Scripps Institution of Oceanography, La Jolla, California

Key Points:

- Increases in significant wave height (SWH) during boreal and austral spring and summer months is present in most wind anomaly regions
- Magnitude of SWH increase is determined by local conditions within wind anomaly region
- Probability of swell decreases during wind anomaly events implying SWH increase occurs due to locally forced waves

Corresponding author: Sarah T. Gille, sgille@ucsd.edu

Corresponding author: Ana B. Villas Bôas, avillasb@ucsd.edu

12 **Abstract**

13 Significant wave height (SWH) provides insight about the interactions between the
 14 ocean and the atmosphere. In the Northern and Southern Hemispheres, wave heights have
 15 been observed to undergo an annual sinusoidal cycle in response to seasonal changes in
 16 storm patterns. In the California coast region, local expansion fan wind events lead to
 17 deviations in SWH annual cycle during boreal spring and summer. Other coastal regions
 18 where supercritical channel flows occur during the early summer months due to similar
 19 coastal topography and atmospheric forcing s to California include eastern boundary re-
 20 gions of ocean basins, the south Caribbean, and West Arabian Sea. Here, intraannual
 21 variability of surface gravity waves is analyzed globally in SWH and wind speed data,
 22 using over two decades of satellite-derived SWH and wind data. The location at which
 23 surface waves are generated is used for validation of mechanisms driving wave charac-
 24 teristics. Phasing of the SWH seasonal cycle reveals that the primary hemisphere dom-
 25 inating the wave field has an abrupt and rough boundary through the equatorial region
 26 due in part to topography causing shadowing of waves. In summer wind anomaly (SWA)
 27 regions, the fraction of wave variability attributed to local wind events varies depend-
 28 ing on local conditions. Global maps of probability of swell based on wave age confirm
 29 that wind anomaly regions typically have locally forced waves during the spring and sum-
 30 mer months.

31 **1 Introduction**

32 Surface gravity waves are fundamental to our understanding of the interactions be-
 33 tween the ocean and atmosphere, including the exchange of momentum, heat, gasses, and
 34 energy (Cavaleri et al., 2012; Edson et al., 2007; Sullivan et al., 2004). The flux of mo-
 35 mentum and energy from the wind to the wave field is the principal generation mech-
 36 anism of ordinary surface waves (Ardhuin, 2018), which are commonly defined as hav-
 37 ing wave periods between 1 to 30 seconds and being predominantly generated by the wind
 38 (Munk, 1951). These waves can propagate long distances across the oceans away from
 39 their generation site (Snodgrass et al., 1966); thus, the wave field in a particular loca-
 40 tion is usually composed by the superposition of locally and remotely forced waves, also
 41 known as wind-sea and swell (Sverdrup & Munk, 1947; Semedo et al., 2011; Jiang & Chen,
 42 2013; Villas Bôas et al., 2017).

43 Previous studies have analyzed the temporal and spatial variability of ocean winds
 44 and waves on a global scale with the use of satellite remote sensing and models. Young
 45 (1999), for example, used satellite remote sensing and model predictions to investigate
 46 the global variation of wave and wind conditions such as significant wave height (SWH)
 47 and wind speed (WSP) and showed that the wave and wind conditions fluctuate season-
 48 ally with largest observations in the high latitudes. SWH is expected to vary from sum-
 49 mer to winter in response to the seasonal variability of storm systems; thus, establish-
 50 ing a seasonal or annual cycle. Stopa (2019) has recently investigated the seasonal cy-
 51 cle of WSP and SWH on a global scales by systematically identifying seasons and de-
 52 scribing the seasonal statistics of the intraannual variability such as spring and autumn
 53 slopes and length of seasons. The author concluded that there are intricate seasonal pat-
 54 terns observed in each ocean basin and that the energy or variance associated with the
 55 annual and semi-annual cycles illustrates the general structure of temporal variability
 56 in regions. However, other temporal variability with higher and lower frequencies than
 57 the seasonal and semi-seasonal cycles are also present in SWH time series. Echevarria,
 58 Hemer, and Holbrook (2019) extended Young (1999) global analysis using directional wave
 59 spectra from WAVEWATCH III hindcast to illustrate more fully the intraannual or sea-
 60 sonal variability of the global wave field for multiple wave modes generated from par-
 61 ticular synoptic atmospheric forcings. Studies have also focused on global views of the
 62 wind sea and swell climate using satellite remote sensing and model hindcast and reanal-

ysis data over relatively large time periods (Young et al., 2011; Jiang & Chen, 2013; Semedo et al., 2011; Zheng et al., 2016; Stopa & Cheung, 2014b). For example, Semedo et al. (2011) investigated the intra and interannual variability of spectrally partitioned wind sea and swell SWH and showed that global oceans are strongly dominated by swell. Despite the extensive and comprehensive research preformed on the global scale, there is a lack of regional analysis on the wave field in order to look at how the wave field in many regions of the world oceans is strongly influenced by regional-scale wind variability.

Villas Bôas et al. (2017) analyzed how regional-scale wind variability can cause deviations from the SWH seasonal cycle to arise in the temporal variability of SWH. Villas Bôas et al. (2017) explored a distinct deviation occurring in the California coast region due to a local wind phenomena called expansion fan winds (EFWs) which forms due to atmospheric conditions and coastal topography (Winant et al., 1988). This deviation is characterized as an increase or simply a bump in SWH during the spring and early summer months due to local EFW events generating locally forced waves that dominate the wave field (Villas Bôas et al., 2017). This same supercritical channel flow has been hypothesized by Winant et al. (1988) to be present in other oceanic regions that have coastal topography and atmospheric conditions similar to California. These regions include the west coast of Australia, the coast of Namibia in southern Africa, the coast of Chile, the southern Caribbean sea, the northwest coast of Africa near Morocco, and in the Arabian sea near the tip of Somalia. These regions are a combination of eastern boundary current regions (EBRs), monsoon regions, and regions significantly sheltered from remotely forced waves. Hereon they will be referred collectively as summer wind anomaly (SWA) regions. There has been no exploration of the possible effects on the intraannual variability of SWH in SWA regions from the regional-scale wind variability generated from EFWs. This is the goal of our paper.

By analyzing intraannual variability of SWH for surface gravity waves and WSP on a global scale from 1993 to 2015 using satellite remote sensing, we investigate SWA regions to determine if the same seasonal cycle deviation as in the California Coastal region is present and if a corresponding maximum in wind speed seasonal cycle is correlated to the SWH deviation. In addition, the structural distribution of the parameters of the annual and semi-annual cycle on a global scale is explored in order to give insight into the general forcing mechanisms and parameters of the wave field influencing these deviations in SWH. In order to justify that SWH during the spring months in these SWA regions are locally forced, wave age can be used for separating growing seas from fully developed seas for collocated WSP and SWH data. We assess SWA regions in order to understand remote versus local forcing effects on the dominate characteristics of the wave field. This can lead to a deeper understanding of the wave climate and sea-state in these partially wind-sea dominated regions and aids in improving model representations of the wave field and gives possible expectations for prevailing sea-state dependent air-sea fluxes (Boas et al., 2019). Practical applications involve coastal shipping and navigation within SWA regions.

This paper is organized as follows. Section 2 explains the data sets used to conduct the time series analysis of global SWH data and the limitations of our analysis. Section 3 explores the general parameters of the annual and semi-annual SWH and WSP models for the entire time series globally as well as regional climatologies in order to demonstrate the relationship between the deviations from the seasonal cycle and the maximum in the WSP seasonal cycle. Section 4 uses wave age in order to illustrate that SWH measurements during the spring and summer months within SWA regions are observing wave fields dominated by locally forced wave rather than remotely forced wave justifying the claim that local wind events cause the deviation from the seasonal cycle. Section 5 summarizes conclusions.

114 **2 Methods**

115 **2.1 Remotely sensed Data**

116 Wave data used in this study are drawn from two decades of cross-calibrated satel-
 117 lite altimeter SWH measurements produced by the Institut français de recherche pour
 118 l'exploitation de la mer (Ifremer). Ifremer's along track cross calibrated SWH altimeter
 119 data was collected from multiple near pole non-sun synchronous satellites over the
 120 time period of 1 January 1993 to 31 December 2015. Comparison of altimeter data against
 121 in situ buoy observations was performed to validate Ifremer data. Here, we binned the
 122 daily along track data onto a 1° by 1° spatial grid. Satellites incorporated in this Ifre-
 123 mer product include ERS-1&2, TOPEX-Poseidon, GEOSAT Follow-ON (GFO), Jason-
 124 1, Jason-2, ENVISAT, Cryosat and SARAL AltiKa (Croiz-Fillon, 2017).

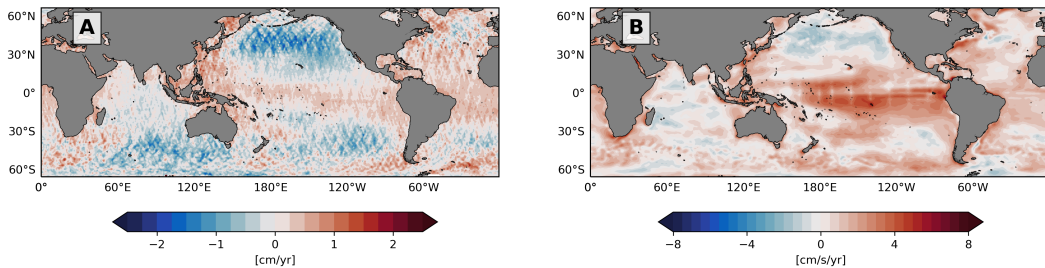
125 Wind data for this study is from the Cross Calibrated Multi-Platform version 2 (CCMP2)
 126 wind vector analysis data produced by Remote Sensing Systems. CCMP2's data prod-
 127 uct is released on a 0.25° by 0.25° spatial grid with 6 hourly temporal resolution. For
 128 this analysis, we averaged CCMP2 winds spatially on a 1° by 1° grid and temporally to
 129 daily resolution in order to match the Ifremer gridded SWH data. The CCMP2 prod-
 130 uct incorporates measurements from active scatterometers, passive radiometers, in situ
 131 buoys, and modelled wind velocity data (Atlas et al., 2011). CCMP reports wind in zonal
 132 and meridional components (Atlas et al., 2011), which are used to compute WSP.

133 The Ifremer SWH product is not co-located temporally with the CCMP2 wind prod-
 134 uct; typical time differences are on the order of 6 hours. For point-to-point analysis, this
 135 would present a major obstacle due to the fact sea state parameters including SWH and
 136 atmospheric conditions including WSP are highly variable on time scales of minutes to
 137 hours, meaning that SWH and WSP can change significantly within a 6 hour period. There-
 138 fore, the WSP measurement at a given location could have no relation at all to a SWH
 139 measurement taken 6 hours later at the same location. The analysis done in this study
 140 focuses on monthly averaged SWH and WSP to allow comparisons between these two
 141 parameters.

142 **2.2 Annual and Semi-Annual Model and Regional Climatology Anal-**
 143 **ysis**

144 In order to analyze the annual and semi-annual variability of SWH and WSP at
 145 each grid point, we least-squares fitted SWH and WSP with a five parameters includ-
 146 ing the mean with annual and semi-annual sinusoidal cycles.

147 The linear trend within the SWH and wind speed time series was addressed within
 148 our analysis by detrending the WSP and SWH monthly data before computing the model
 149 and its parameters. To inspect the magnitude of the linear trend in the data, the least-
 150 squares fit mentioned above with a sixth term accounting for a linear trend was fitted
 151 to the data. The coefficient for linear trend term was used to give a rudimentary mag-
 152 nitude and significance of the linear trend Young et al. (2011). Fig 1 displays globally
 153 the magnitude of the linear trend computed over the time period of 1 January 1993 to
 154 31 December 2015 for SWH and WSP. This illustrates that the magnitude of the linear
 155 trend for SWH and WSP is temporally varying on the order of centimeters and centime-
 156 ters per sec respectively whereas the seasonal cycle is temporally varying on the order
 157 of meters or meters per sec respectively. This means the linear trend's temporal vari-
 158 ation is two order of magnitude smaller than the temporal variation of the annual and
 159 semi-annual cycle. The linear trend magnitudes are slightly less than reported by Young
 160 et al. (2011). Whether the linear trend is an artifact of the cross calibrated multi-platform
 161 data sets or is physically authentic, we do not know. However, the linear trend is removed
 162 for completeness.



163 **Figure 1.** Magnitude of linear trend for monthly averaged (A) Ifremer SWH and (B) CCMP2
164 WSP.

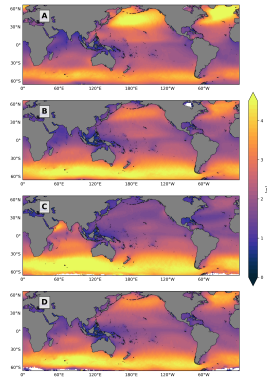
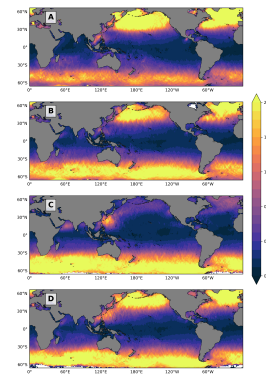
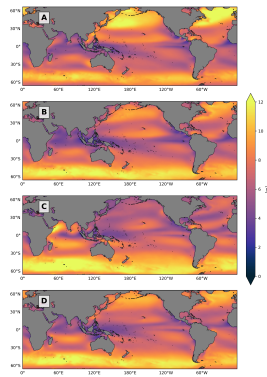
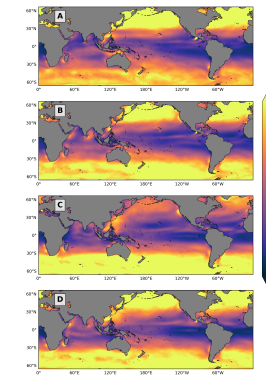
165 The parameters used to evaluate and compare the annual and semi-annual cycles
166 spatially were the amplitude and phase constant. Amplitude and phase constant is com-
167 puted individually for the annual and semi-annual cycle of SWH and WSP. In order to
168 evaluate the goodness of fit of the model, the coefficient of determination is used. The
169 coefficient of determination quantifies the percent of variance of the data explained by
170 the model.

171 For the climatological analysis within SWA regions, SWH and WSP grid points within
172 4° by 4° square regions were first temporally averaged into single monthly averages and
173 then spatially averaged. Therefore, we obtain SWH and WSP climatologies for the en-
174 tire region in order to compare when the bump in SWH climatology and the maximum
175 in the WSP climatology occur with respect to each other. The 4° by 4° regions were picked
176 by looking at seasonally averaged WSP maps within SWA regions. 4° by 4° regions that
177 had anomalously high WSP and small spatial WSP gradients were chosen as seen in
178 Fig 9 and Fig 10. For the northern hemisphere, the seasonal average from the boreal sum-
179 mer was used in order for the high WSP anomaly to be present in SWA regions. Like-
180 wise for the southern hemisphere, the seasonal average from the austral summer was used.
181 Small spatial WSP gradient regions were favorable because the climatology analysis should
182 be performed in regions with consistently high amplitude WSP maximum observations
183 in order to have the highest likelihood of the wave field has significant influence by lo-
184 cal winds. If we spatially averaging over a regions including grid points with high and
185 low seasonally averaged WSP values, then our averaging would include two domains with
186 very different time variability leading to piece-wise rough climatologies. In addition, de-
187 cently sized regions to spatially average data were used to bring down some of the noise
188 present in SWA regions.

189 Seasonal progression maps of the first two statistical moments for Ifremer SWH and
190 CCMP2 WSP data are computed in order to gain insight into the seasonal evolution and
191 variance of the data (Fig 2.2 and Fig 2.2).

196 2.3 Limitations of Data

197 The data used in this study has limitations associated with Ifremer and CCMP2
198 data product admonitions, the use of integral parameters instead of spectral data, and
199 land contamination. Ifremer's SWH data product has been validated by Queffeulou (2004)
200 by comparing SWH measurements with in situ buoy observations and ensuring near ho-
201 mogeneity of SWH measurements between satellite missions. However, high magnitude
202 SWH data from altimeters still underestimates SWH when compared to in-situ obser-
203 vations. The CCMP2 cross calibration and assimilated surface wind data may contain
204 spurious trend due to assimilation process of modelled ECMWF data and underestima-
205 tion of wind speeds in high wind regions due to modelled ECMWF winds tendency to

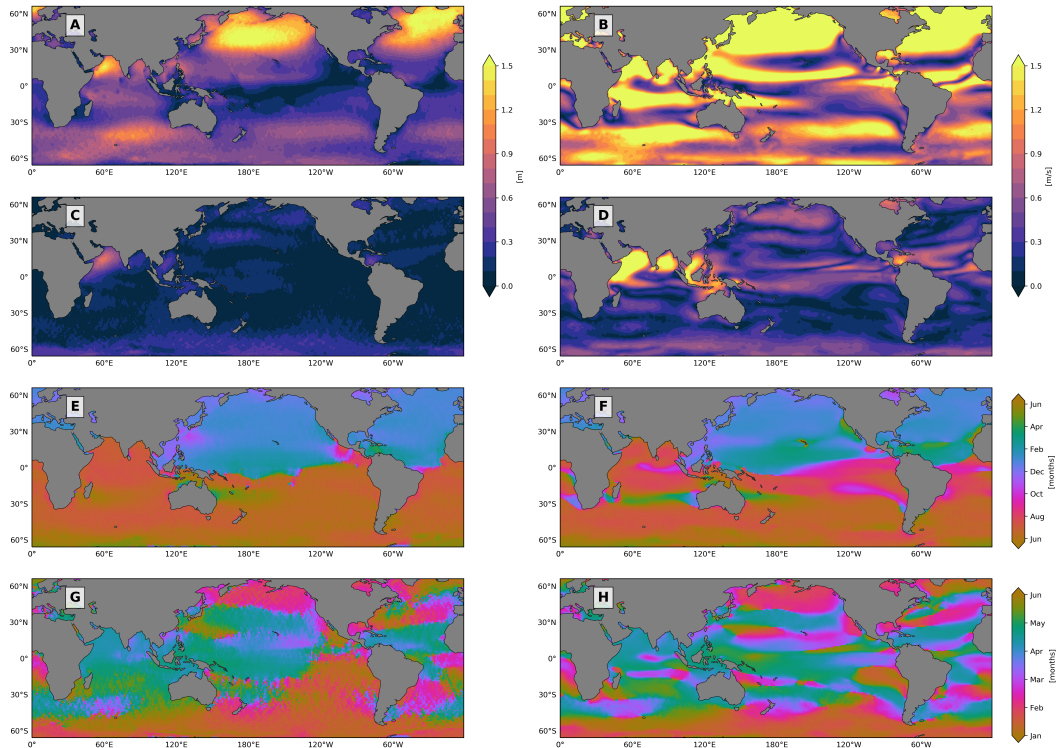
192 **Figure 2.** Ifremer SWH Seasonal Mean**Figure 3.** Ifremer SWH Seasonal Variance194 **Figure 4.** CCMP2 WSP Seasonal Mean**Figure 5.** CCMP2 WSP Seasonal Variance

206 underestimate wind speed (Atlas et al., 2011). The annual and semi-annual cycles are
 207 stronger signals present in the WSP climate in SWA regions and would therefore not be
 208 effected by spurious trends. However, underestimation of WSP could have effects on
 209 the analysis of SWA regions where the wind anomaly occurs. Integral parameters are
 210 used in this analysis with the understanding of its limited ability to full describe all wave
 211 systems present in the wave field. Echevarria et al. (2019) highlight this shortcoming of
 212 integral parameters in wave climatology analysis and present a climatological analysis
 213 of multimodal directional wave spectrum via principal component analysis of the spec-
 214 tral data from Wave Watch 3 ECMWF reanalysis data. Semedo et al. (2011) also used
 215 Wave Watch 3 ECMWF reanalysis data in order to analyze the global wave climate. Lastly,
 216 satellite altimetry data in near coastal region on the scales of 10km to 100km off shore
 217 should be neglected from the analysis due to the data being possible contaminated by
 218 land. Fortunately, the local wind anomalies persist for several hundreds of kilometer off
 219 shore allowing reliable SWH and WSP data satellite data to be recorded (Winant et al.,
 220 1988).

221 3 SWH and WSP Intraannual Variability Analysis

222 223 3.1 Global parameters of Annual and Semi-annual Model and Implications to SWA Regions

224 Figure 6 compares the Ifremer SWH annual and semi-annual cycle amplitude and
225 phase with CCMP2 WSP results. Notice that the phase has been converted from radi-
226 ans to months



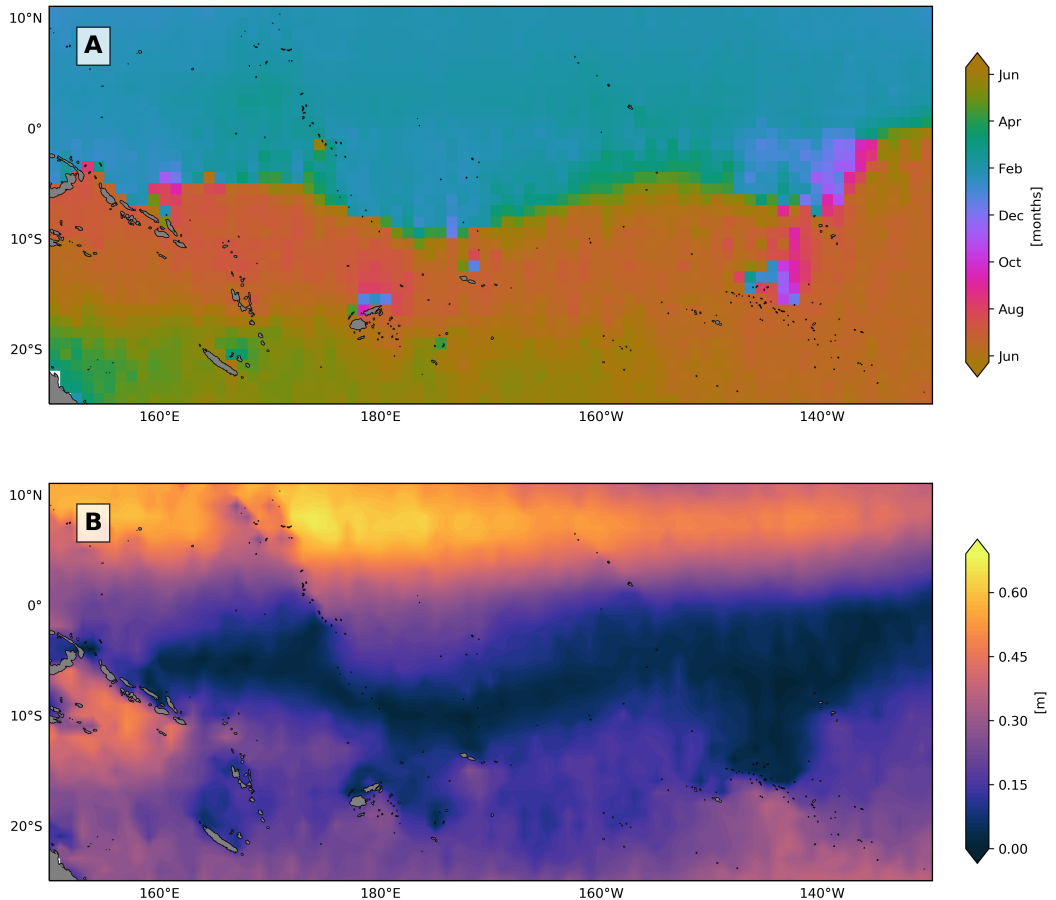
227 **Figure 6.** Amplitude of annual cycle for (A) Ifremer SWH and (B) CCMP2 WSP; amplitude
228 of semi-annual cycle for (C) Ifremer SWH and (D) CCMP2 WSP; phase of annual cycle for (E)
229 Ifremer SWH and (F) CCMP2 WSP; phase of semi-annual cycle for (G) Ifremer SWH and (H)
230 CCMP2 WSP. See text for details of computation.

231 The annual cycle phase map for SWH (Fig. 6E) shows that the phase of the sea-
232 sonal cycle in the Northern Hemisphere is approximately 6 months out of phase with the
233 Southern Hemisphere, with the timing of maximum wave height well aligned with the
234 timing of maximum WSP seasonal cycle (Fig. 6F). WSP is a common characteristic of
235 synoptic high latitude storm systems in the northern and southern hemisphere and ex-
236 periences a seasonal cycle (Fig. 4). Remotely forced waves generated from these near sur-
237 face winds will propagate away from these storm systems throughout ocean basins and
238 will predominately dominate the wave field (Semedo et al., 2011). This causes SWH of
239 these remotely forced waves to undergo a similar seasonal cycle (Fig. 2). Therefore, this
240 6-month phase shift illustrates that storm systems' annual frequency and intensity cy-
241 cles in the mid to high latitudes of the Northern and Southern Hemispheres set the sea-
242 sonal cycle of SWH. However in some regions where local wind events input a significant
243 amount of energy into the ocean, the SWH may become dominated by locally forced waves.

244 Other features in the SWH annual cycle phase map include higher spatial variability
 245 in the Southern Hemisphere than in the Northern Hemisphere, potentially due to the
 246 nontrivial wind systems present in the Southern Hemisphere experiencing high amplitude
 247 intraannual variability. The intraannual variability of storm system would directly
 248 effect the wave climate because remote and local storms or prevailing winds are one of
 249 the main forcing mechanisms generating these wind waves. Therefore, high spatial variabil-
 250 ity in phase exists in the southern hemisphere. In the equatorial region, the domi-
 251 nant phase changes roughly along a line where the amplitude of the seasonal cycle tends
 252 towards zero (Fig 6A). This boundary designates the transition from the seasonal cy-
 253 cle being primarily set by storm system originating in the Northern hemisphere to be-
 254 ing primarily set by storm systems originating in the Southern Hemisphere. This smooth
 255 transition is expected in the region where the amplitude tends towards zero. This phase
 256 boundary in the Pacific and Atlantic is also known as a swell front (Young, 1999) and
 257 is the boundary between domains of dominance of swell from each hemisphere and dis-
 258 cussed in Semedo et al. (2011) and Jiang and Chen (2013). However, waves propagat-
 259 ing from the Northern and Southern Hemispheres coexist superimposed on the wave field
 260 at and beyond the swell front (Echevarria et al., 2019). This means that the waves will
 261 continue propagating in their respective directions into the opposite hemisphere.

262 In the tropical Pacific, several abrupt shifts in phase exist between 10° and 20° south
 263 at approximately 180°E and 145°W (Figure 7). One explanation for these abrupt phase
 264 shifts is island shadowing. Waves from the Southern Ocean propagating northward en-
 265 counter the topography of Polynesian islands and break and dissipate on the shores fac-
 266 ing the direction of the oncoming waves. The opposite side of the island does not encounter
 267 any of these remotely or locally forced waves. Therefore, the southern facing sides of these
 268 islands are in phase with the Southern Hemisphere seasonal cycle while the northern fac-
 269 ing sides of the islands are in phase with the northern hemisphere because they are only
 270 exposed to southward traveling waves originating in the Northern Hemisphere. Some waves
 271 are able to refract between these islands as well. Waves from the Southern Ocean that
 272 are able to propagate through the Polynesian islands continue into the northern Pacific.
 273 Evidence for this northward propagation can be seen in a tongue of slightly higher phase
 274 constant value between the two indentations present on the phase boundary at approx-
 275 imately 175°E and 140°E (Figure 7A). Higher phase constant value refers to the max-
 276 imum of the SWH annual cycle occurs during the spring months of May or April as
 277 it shifts towards the boreal winter.

280 The phase transition from the Northern Hemisphere dominated domain to the South-
 281 ern Hemisphere dominated domain occurs slightly south of the equator between 5° and
 282 10°S in the west pacific staring at 170°W , and it slowly shifts equatorward while mov-
 283 ing east across the Pacific (Figure 7A). Explanations for the geographic location of the
 284 boundary are linked to where the amplitude of the seasonal cycle tends to zero (Figure 7B).
 285 Other explanations include the following. Waves would encounter westward flowing south
 286 equatorial current (SEC), south equatorial countercurrent (SECC), the westward north
 287 equatorial current (NEC), or the north equatorial countercurrent (NECC). The SEC and
 288 SECC are located on average closest to the phase boundary, and they are known to be
 289 present between 5° and 10°S (Talley, 2011). However, the wave-current interactions be-
 290 tween waves propagating into this region from the Northern and Southern Hemisphere
 291 have no effects of wave propagation when the velocities of the two are orthogonal. In ad-
 292 dition, the wave-current interaction is on small scales and would be undetectable in satel-
 293 lite altimeter SWH data when the footprint of the satellite covers several kilometers of
 294 sea surface. Additionally, the phase boundary of the annual cycle does not line up with
 295 the intertropical convergence zone (ITCZ) characterized as a low pressure system with
 296 heavy precipitation and deep convection (Schneider et al., 2014) that causes very calm
 297 sea surface conditions. These calm sea surface conditions could be thought of as being
 298 associated with the low amplitude seasonal cycle region. However, low amplitude does
 299 not imply low SWH values because there is a mean value that offsets the SWH seasonal



278 **Figure 7.** (A) Ifremer SWH Annual cycle phase map in Polynesian island region illustrating
279 island shadowing, (B) Ifremer SWH annual cycle amplitude map in Polynesian island region

300 oscillations from zero. By looking at the SWH seasonal mean (Fig 2), the mean is rel-
301 atively low, but not the minimum value of the equatorial region. In addition, the intertrop-
302 ical convergence zone annual migrates between 9°N in boreal summer and 2°N in bo-
303 real winter in the central Pacific following the warmer hemisphere (Schneider et al., 2014).
304 This is significantly far from the phase boundary. Wave to wave interactions and non-
305 conservative forcing could possible play a significant role here; however, the angle between
306 each wave's group velocity determines significantly how energy and momentum will be
307 distributed throughout the system. By looking at fig 7, we see that islands within this
308 region play a significant role in setting the shape of the minimum annual cycle ampli-
309 tude region for SWH. Islands outline the near zero contour for amplitude and therefore
310 significantly affect how waves propagate into this region and how those waves will in-
311 teract with each other.

312 Other interesting structures exist in near coastal regions and in the Atlantic in Fig. 6E.
313 In the Atlantic, there is also a smooth phase boundary transition with one abrupt phase
314 shift close to the western side of the Atlantic. On the western side, the phase boundary
315 is almost vertical following a line of constant latitude. This dynamic boundary also oc-
316 curs in the zero amplitude SWH seasonal cycle region and is slightly below the equator.
317 In addition, just off the coast of Mexico, there is an out of phase region that is close to
318 the near zero amplitude region. These other structures will be left for further research.

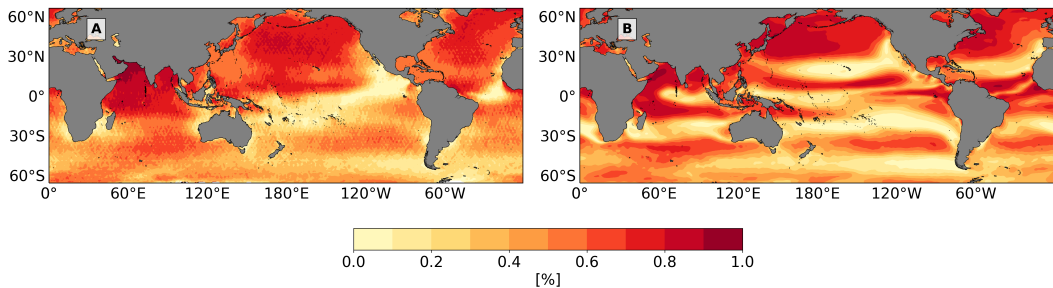
319 The SWH and WSP annual cycle phase maps display an interesting relationship
 320 between deviations in the SWH seasonal cycle and local wind anomalies that are gen-
 321 erated by similar mechanics to expansion fan wind events off the California coast. In the
 322 SWH annual phase constant maps, deviations from the seasonal cycle predominantly can-
 323 not be observed in the cases when the deviation in the seasonal cycle is less than the max-
 324 imum values of the seasonal sinusoidal oscillations. However, this is not the case for all
 325 SWA regions, as will be explained later.

326 For the WSP annual cycle phase map (Fig. 6F), the phase constant clearly outlines
 327 regions where local wind anomalies similar to the EFW events off the coast of Califor-
 328 nia are present. The wind anomalies are characterized on the phase map by a π phase
 329 shift in the WSP seasonal cycle or a 6 month shift is the WSP seasonal cycle maximum
 330 from the surrounding region. By looking at the global map of phase for WSP, we observe
 331 that SWA regions typically are out of phase with their surrounding regions. For exam-
 332 ple, in the EBR off the coast of Australia (Fig 6F), the phase reveals that the maximum
 333 in the WSP seasonal cycle occurs during the austral summer within the SWA region. Out-
 334 side of the SWA region, WSP reaches a maximum during the austral winter.

335 The WSP phase map has structural similarities to the SWH phase map due to the
 336 proportional relationship between wind waves and the storm systems that generate them:
 337 the Northern and Southern Hemispheres are six months out of phase with each other,
 338 and the Southern Hemisphere has more spatial variability (Fig 6F). These intricate South-
 339 ern Hemisphere features are due to the dynamic intraannual variability of storm systems
 340 especially in the Indian ocean (Schott et al., 2009). However, there are many differences
 341 between SWH and WSP phase maps. The phase boundary in the Pacific designating the
 342 transition in the hemisphere that is primarily setting the WSP seasonal cycle is further
 343 north, and the majority of the boundary is smooth and continuous, without abrupt changes
 344 in phase on the eastern side of the Pacific, but with a slightly high gradient on the west
 345 side. In the Atlantic, the phase boundary is a smooth transition and is more linear in
 346 shape than the SWH phase boundary in the Atlantic. The phase boundary in the At-
 347 lantic follows closely the near zero WSP amplitude of the annual cycle; however, in the
 348 Pacific, the amplitude does not tend to zero near or at the equator. Furthermore, the
 349 Indian Ocean has prominent structures of swooping fingers of high phase constant val-
 350 ues which are again due to dynamics of intraannual variability of storm system and pre-
 351 vailing winds (Schott et al., 2009).

352 Coefficient of determination global maps can be used to assess the percentage of
 353 the variability explained by the model in order to understand whether there are other
 354 processes not accounted for by the annual and semi-annual cycles. Fig 8 shows that the
 355 percent of variability explained by the model is high in the North Pacific and Atlantic
 356 and low in the Southern Ocean for SWH and WSP. For SWH, the percent variation ex-
 357 plained reaches a minimum in the near-equatorial region in the Pacific and Atlantic. For
 358 WSP, the features of high percent variation explained are complex throughout the equa-
 359 torial region with varying amounts from near 100% to near 0%. These low values in the
 360 equatorial region may be attributed partly to the decadal oscillation of El Niño. The per-
 361 cent variation varies for each SWA region. For both SWH and WSP, SWA regions range
 362 from having 10% to 40% of the variation explained by the two modes represented in the
 363 model with the exception of the Arabian and Caribbean seas which have near 100% vari-
 364 ation explained. There are especially low values off the coast of Chile and Namibia for
 365 SWH and off the coasts of California, Chile, and North Africa for WSP. The Arabian
 366 and South Caribbean seas have higher percent variation explained by the model because
 367 these regions primarily have wave and wind forced by mechanics that have annual and
 368 semi-annual frequencies. In support of this argument, both of the coefficient of deter-
 369 minations geographic features follow very closely with features in the annual and semi-
 370 annual amplitude of SWH and WSP maps such that the percent of variation explained
 371 by the model is highest in regions with high amplitude and lowest in region of near zero

372 amplitude. This means that the model explains the variability significantly less in most
 373 of the SWA regions because there are weak annual and semi-annual cycles. In addition,
 374 there are other forcing mechanism at work in these regions that contribute more signif-
 375 icantly to the wave and wind field. One of these forcing mechanisms for the wave field
 376 is the deviation from the seasonal cycle from local wind events. The goodness of fit quan-
 377 tified by the coefficient of determination should not be thought of as a test of reliabil-
 378 ity of the model. Rather, it is an indication of physical processes not accounted for by
 379 the model, which we want to explore to understand the underlying mechanisms gener-
 380 ating the variability in the wave and wind fields.

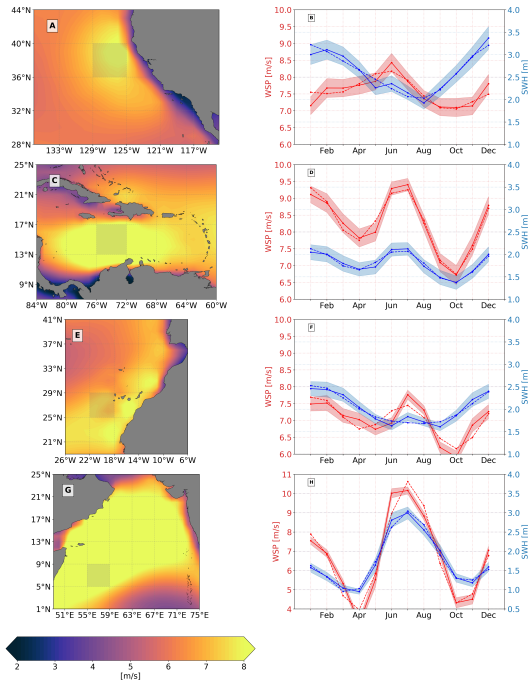


381 **Figure 8.** Global map of Coefficient of determination for Ifremer SWH (A) and CCMP2
 382 WSP (B) using Unweighted Annual and semi-annual Least Square Fit from January 1st, 1993 to
 383 December 31st, 2015 for a metric of the goodness of fit of the model.

384 3.2 Regional Climatologies of SWA Regions

385 In order to obtain a closer look at the seasonal cycle within these SWA regions, cli-
 386 matologies or monthly mean SWH and WSP time series were computed from January
 387 1st, 1993 to December 31st, 2015 within 4° by 4° grid boxes. Fig 9 and Fig 10 show the
 388 regional climatologies from SWA regions in the Northern and Southern Hemispheres re-
 389 spectively as well as the 4° by 4° regions within each SWA regions where the climatol-
 390 ogy is computed. From these climatologies, a clear difference is seen between Northern
 391 and Southern Hemisphere SWA regions.

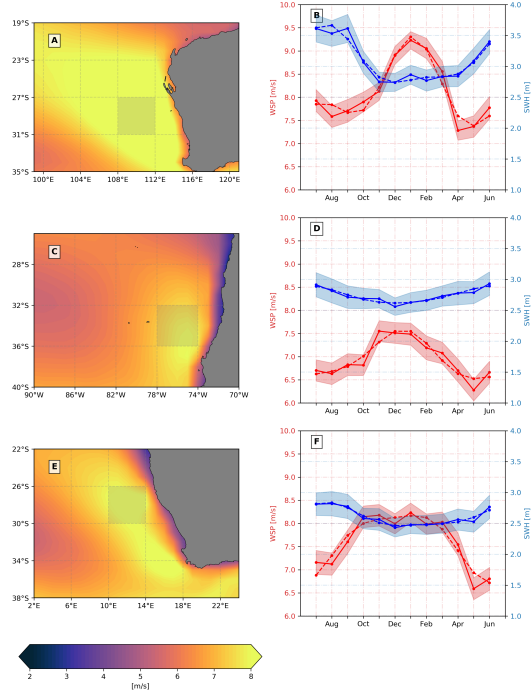
406 In all Northern Hemisphere SWA regions, the maximum in the WSP climatology
 407 occurs at the same time, when a deviation from the sinusoidal SWH seasonal cycle oc-
 408 curs. Examples include the Northern California and North African SWA regions (Fig 10B,F).
 409 Off the coast California, the WSP seasonal cycle reaches a maximum during the month
 410 of June. This peak is associated with an increase in SWH at the same time that the sea-
 411 sonal cycle is reaching a summer minimum. In the North African region off the coast of
 412 Morocco, a WSP maximum and a deviation from the SWH seasonal cycle are present
 413 in the month of July. In the Southern Hemisphere, the maximum in the WSP occurs dur-
 414 ing the austral summer in SWA regions, however there is only a small magnitude devi-
 415 ation from the SWH seasonal cycle occurring at the same time in the SWH climatology.
 416 Off the coast of western Australia (Fig 10B), a small magnitude deviation from the SWH
 417 annual cycle is present during the month of February when the maximum in the WSP
 418 climatology occurs. However, off the coast of Chile and Namibia (Fig 10D,F), deviations
 419 from the seasonal cycle are not present at all in the SWH climatology. Therefore, we pro-
 420 pose that Southern Hemisphere SWA regions' (Fig 10) local wind forcing have compar-
 421 atively less pronounced influence on the wave climate than in the Northern Hemisphere.
 422 This is presumed to occur because the magnitude of the deviation in the SWH cycle is
 423 determined by the local conditions and characteristics of the wave field within the re-
 424 gion. Local conditions refers to the exposure and distance of the SWA region from re-



392 **Figure 9.** SWA regional maps of WSP averaged over the months of June, July, and August
 393 (left column) with Ifremer SWH (solid blue curve) and CCMP2 WSP (solid red curve) climatolo-
 394 gies in shaded 4° by 4° boxes within SWA regions located in the Northern Hemisphere. Shading
 395 in climatologies represents the standard error of the mean and dotted blue and red lines are the
 396 annual plus semi-annual cycle least-squares fitted to monthly climatology for SWH and WSP
 397 respectively. SWA regions include Northern California (A and B), Southern Caribbean Sea (C
 398 and D), North Africa near the coast of Morocco and western Sahara (E and F), North-Western
 399 Arabian Sea (G and H)

425 mostly forced waves generation regions. In other words, how sheltered the SWA region
 426 is to regions with storms that produce high SWH remotely forced waves. By looking at
 427 looking at the two extreme cases of heavy sheltering and high exposure, the magnitude
 428 of the deviation from the SWH seasonal cycle can be explained.

429 In the southern Caribbean Sea, the SWH climatology is in phase with the WSP
 430 climatology in Fig 9D. This implies that local wind events, including the wind anomaly
 431 during boreal summer and other wind events, predominately generate the waves within
 432 the region. This is due to the SWA region having little exposure to waves propagating
 433 from the high latitudes of the northern or southern Atlantic resulting in little of the wave
 434 energy being remotely forced. This sheltering from remotely forced waves is due to the
 435 Caribbean islands that ring the Caribbean sea (Fig 9C). The resulting seasonal variabil-
 436 ity, including the annual and semi-annual cycles, of this region is thus primarily set by
 437 local wind events within the Caribbean sea. Now by analyzing the increase in SWH oc-
 438 ccurring during the boreal summer due to the wind anomaly, the magnitude of this in-
 439 crease in SWH is relatively large such that the local maximum in SWH during the bo-
 440 real summer is of similar or equal magnitude to the local maximum of the annual cy-
 441 cle. Therefore, the local wind anomaly significantly alters the climatology of SWH be-
 442 cause the wave field tends to be dominated by locally forced wave for the majority of the
 443 year. This increase in SWH due to the wind anomaly also causing two maxima in SWH
 444 per year. This explains the near out of phase values seen in the Caribbean sea with re-



400 **Figure 10.** SWA regional maps of WSP averaged over the months of December, January, and
 401 February (left column) with Ifremer SWH (solid blue curve) and CCMP2 WSP (solid red curve)
 402 climatologies in shaded 4° by 4° boxes within SWA regions located in the Southern Hemisphere.
 403 Shading and dotted lines are as in Fig. 9. SWA regions include Western Australia (A and B),
 404 Central Western coast of South America near Chile (C and D), and South-Western Coast of
 405 Africa near Namibia (E and F)

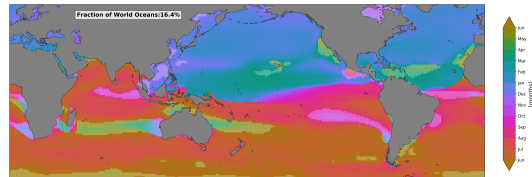
445 spect to the rest of the Northern Hemisphere (Fig 6E). In addition, in Fig 6C,D, the large
 446 semi-annual cycle in the SWH and WSP semi-annual amplitude maps is clearly seen in
 447 the South Caribbean Sea due to the local wind anomaly. A similar semi-annual pattern
 448 occurs in the Arabian and South China seas, where monsoon winds generate high locally
 449 forced waves. The Arabian Sea has a similar wave climate to the South Caribbean with
 450 the wave field having a high tendency to be dominated by locally forced waves, however,
 451 this SWA region is not sheltered from remotely forced waves that propagate up from the
 452 Southern Ocean. This examples the high magnitude increase in the SWH climatology
 453 during boreal summer (Fig 9H).

454 Off the coast of Western Australia, the increase in the SWH climatology during aus-
 455 tral summer has small magnitude due to this SWA region having high exposure to the
 456 Southern Ocean where larger storms produce larger SWH remotely forced waves. These
 457 waves propagating into the SWA region cause there to be a high mean SWH which the
 458 SWH seasonal cycle oscillates about. These remotely forced waves of large amplitude over-
 459 whelm the wave field within the SWA region and cause the locally forced waves to have
 460 significantly less affect such that locally forced waves are less likely to dominate the wave
 461 field from the remotely forced waves. Therefore, the remotely forced waves overwhelm
 462 the locally forced waves and tend to dominate the wave field for a significant majority
 463 year with a slight exception during January in the austral summer. During January, the
 464 wave field tends to be dominated by locally forced waves and causes the slight increase
 465 in SWH. For the other two SWA regions in the Southern Hemisphere, the wave field is
 466 tends to be dominated by remotely forced waves all year round.

467 We conclude that the magnitude of the deviation in the SWH cycle is determined
 468 by the local conditions and characteristics of the wave field within the region. Conse-
 469 quentially, the magnitude of the deviation from the SWH seasonal cycle is less than North-
 470 ern Hemisphere SWA regions.

471 From each of these climatology of SWA regions (Fig 10, Fig 9), it is also observed
 472 that significance of the deviation varies from region to region. The significance of devi-
 473 ation from the seasonal cycle can be determined by considering the standard error of the
 474 mean (Figs. 9,10). In regions with high variance, the standard error of the mean is large
 475 enough that the deviation from the seasonal cycle is not statistically significant. This
 476 is seen in the west coast of Australia, coast of Chile, and the coast of Namibia. The stan-
 477 dard error of the mean was obtained for each month by calculating the decorrelation time
 478 scale and then computing the number of independent realizations in the SWH and WSP
 479 time series using this decorrelation time scale. National Data Buoy Center's buoy data
 480 off the California (station 46059) and in the southern Caribbean Sea (station 42058) were
 481 used for computing decorrelation time scales. The Northern California decorrelation time
 482 scale was applied to Northern California, Western Australia, North Africa, South Africa,
 483 and Central-West South America because there is a high mixture of wind sea and swell
 484 waves from a large assortment of wave systems entering these regions. The South Caribbean
 485 decorrelation time scale was applied to the Southern Caribbean and Arabian Sea because
 486 there is a significantly large amount of wind sea compared to swell waves in these regions.

487 To comprehend the global extent of anomalous local surface winds over the world
 488 oceans and their possible influences on the local wave field, the fraction of the world's
 489 oceans experiencing anomalous winds was computed using WSP annual cycle phase cal-
 490 culated from CCMP2 daily data. WSP phase is categorized as anomalous when the WSP
 491 phase is greater than $-\frac{\pi}{2}$ in the Northern Hemisphere corresponding to the maximum
 492 in WSP annual cycle occurring outside of boreal winter months and greater than $\frac{\pi}{2}$ and
 493 less than 0 in the Southern Hemisphere corresponding to the maximum in the WSP an-
 494 nual cycle occurring outside of the Austral winter months. Observe that these wind anom-
 495 alies are generated by a broad range of atmospheric forcings other than the expansion fan
 496 wind anomaly focused in this study. In order to compute this fraction, the world oceans
 497 where partitioned into southern and northern hemisphere basins including Indian Ocean,
 498 North and South Pacific, and North and South Atlantic Basins. Marginal Seas were mostly
 499 excluded as well as the equatorial regions across the Pacific and Atlantic oceans. We found
 500 that approximately 16.4% of the world oceans have anomalous high WSP during the spring,
 501 summer and fall months when it would be though to have lower WSP in the region. Fig 11
 502 shows geographically where these wind anomalies occur. This calculation is approximate
 503 and not highly rigorous, however it gives a general impression of the larger extend and
 504 the geographic locations where these wind anomalies occur. All SWA regions are con-
 505 sidered as anomalous except for the Arabian Sea. These regions categorized as having
 506 anomalous WSP phase may have a higher probability of the wave field being dominate
 507 by the local forced waves. However, this is depended on the local conditions of the wave
 508 field during the spring, summer, and fall months as discussed previously.



509 **Figure 11.** WSP annual cycle phase with gridded and lighter regions indicating anomalous
 510 wind regions

511 4 Wind-sea vs. Swell Dominance in SWA Regions

512 4.1 Local vs. Remotely Forced Waves

513 In order to evaluate whether SWA region waves are generated by local wind events
 514 or remote storms, we use wave age information to classify waves as locally or remotely
 515 forced. During a storm, wind blows over a length of ocean surface called fetch at cer-
 516 tain speed and for a given time duration, generating a packet of waves. Initially, waves
 517 that are formed by the wind are categorized as locally forced waves since the atmosphere
 518 is still supplying energy and momentum to the waves. These local forced waves are com-
 519 monly called wind-seas. The frequency or wavenumber spectrum is evolving as wave height,
 520 frequency, and period of the waves grow. These waves tend to have shorter periods (or
 521 high frequency and wavenumber) and thus travel at slower phase speeds than long pe-
 522 riod waves. Ardhuin, Chapron, and Collard (2009) observed swells propagating across
 523 ocean basins using satellite altimetry data from ENVISAT and showed that steep swell
 524 waves lose a significant fraction of their energy (up to 68%) over distances of 2800 km
 525 due to the laminar to turbulent transition in the air-side boundary layer. Wind-sea waves
 526 tend to be steep because of their short periods and high amplitudes, and this leads to
 527 significant dissipation over relatively short distances (Ardhuin et al., 2009). In addition,
 528 wind-sea wave dissipation could also be due to small scale wave-wave interactions, wave-
 529 current interactions and other atmospheric forcing. Therefore, the wind event must be
 530 relatively in close proximity to wind-sea waves. Once the wind is no longer inputting en-
 531 ergy and momentum into the waves, the waves are categorized as remotely forced waves.
 532 Remotely forced waves are commonly called fully developed seas or swell. In the case
 533 of swell waves, the wave field's frequency or wavenumber spectrum is set and is no longer
 534 evolving. These waves tend to have long periods (or low wave frequency and wavenum-
 535 ber) and have the ability to traverse long distances at higher phase speeds than short
 536 period waves (Snodgrass et al., 1966). This leads to the dispersive nature of deep wa-
 537 ter surface gravity waves (Snodgrass et al., 1966).

538 Waves measured by satellite altimeters represent a superposition of local wind waves
 539 and remotely generated swell, and the altimeter does not distinguish frequency, period,
 540 or direction. This is due to shape of the backscatter radiation off the sea surface received
 541 by the satellite altimeter obtaining an average of the variability of the wave height present
 542 in the satellites footprint (Chelton et al., 2001). Therefore, the SWH obtained from sat-
 543 llite altimetry represents the wave height of the dominate waves within the wave field where
 544 these waves may be generated locally or remotely. Globally, the wave field is consistently
 545 dominated by swell (Chen et al., 2002; Semedo et al., 2011).

546 To distinguish between wind-sea and swell waves, wave age may be used. Wave age
 547 quantifies the stage of development of waves and is therefore used to separate locally forced
 548 waves from remotely forced waves through an empirically and theoretically determined
 549 criterion (Alves et al., 2003). The wave age criterion is defined as

$$546 \text{Wave Age} = \frac{C_p}{U_{10}}, \quad (1)$$

550 where C_p is phase speed of the surface gravity wave or the speed of an individual wave
 551 crest and U_{10} is the wind speed 10 meters above the ocean surface. The separation value
 552 used in our analysis to distinguish locally and remotely forced waves is

$$\frac{C_p}{U_{10}} > 1.2 \quad \text{Remotely Forced Waves} \quad (2)$$

$$\frac{C_p}{U_{10}} \leq 1.2 \quad \text{Locally Forced Waves} \quad (3)$$

553 This criterion has been chosen and has empirically shown that wave growth stops or at
 554 least becomes very slow when wave age is greater than 1.2 (Donelan et al., 1992). This
 555 corresponds with waves crests travelling 20% faster than the wind speed 10 meters above

556 the ocean surface, so that the waves are outrunning the wind and not able to receive fur-
 557 ther wind energy input. We assume that the satellite observes deep water waves, with
 558 a wavelength much less than the water depth. For deep water waves, the deep water dis-
 559 pension relationship yields a peak phase speed:

$$C_p = \frac{g}{2\pi f_p} \quad (4)$$

560 4.2 Probability of Swell: Wave Age Method

561 Using wave age or other wind-sea and swell separation techniques, probability of
 562 swell can be obtained to illustrated the amount of times the wave field is swell-dominated
 563 for a given grid point as a fraction of the total amount of wave events which includes wind-
 564 sea dominated and swell dominated events:

$$\text{Probability of swell} = \frac{N_{swell}}{N_{total}} \quad (5)$$

565 where N_{swell} is the number of time steps with wave age exceeding 1.2 representing a swell
 566 dominated wave field and N_{total} is the total number of observations in the time series.

567 Probability of Swell has been computed globally before by Jiang and Chen (2013)
 568 and Semedo et al. (2011). Jiang and Chen (2013) used collocated satellite altimetry SWH
 569 and radiometer WSP from the Jason-1 satellite mission to compute the probability of
 570 swell using a wind-wave relationship derived from the Wave Modeling (WAM) Program
 571 which was able to separate wind-seas from swell. Global seasonal maps of probability
 572 of swell showed that the SWH observations by satellite altimetry are categorized primar-
 573 ily as remotely forced waves in all oceans with lower probability of swell in the South-
 574 ern Ocean, in coastal regions, and along common storms tracks (Jiang & Chen, 2013).
 575 The probability of swell also undergoes a seasonal cycle with a decreasing seasonal cy-
 576 cle amplitude when approaching the equator. This decrease in probability of swell in-
 577 dicates an increase in the amount of wind events generating wind seas that dominate the
 578 wave field. Semedo et al. (2011) computed probability of swell using wave age as the sep-
 579 aration criterion with European Centre for Medium-Range Weather Forecasts Re-Analysis
 580 (ERA-40) wave reanalysis. Semedo et al. (2011) found high probability of swell consis-
 581 tently throughout the world oceans implying that swell dominates the wave field (Semedo
 582 et al., 2011). Building on this analysis, wave energy spectra from ERA-40 was used sep-
 583 arated into wind-sea and swell components using WAM separation frequencies and then
 584 SWH, mean wave period (MWP) and mean wave direction (MWD) were computed for
 585 each components. From seasonal maps of SWH decomposed into swell and wind sea com-
 586 ponents, the swell SWH was found to be always higher than the wind-sea component im-
 587 plying that swell dominates the wave spectra (Semedo et al., 2011).

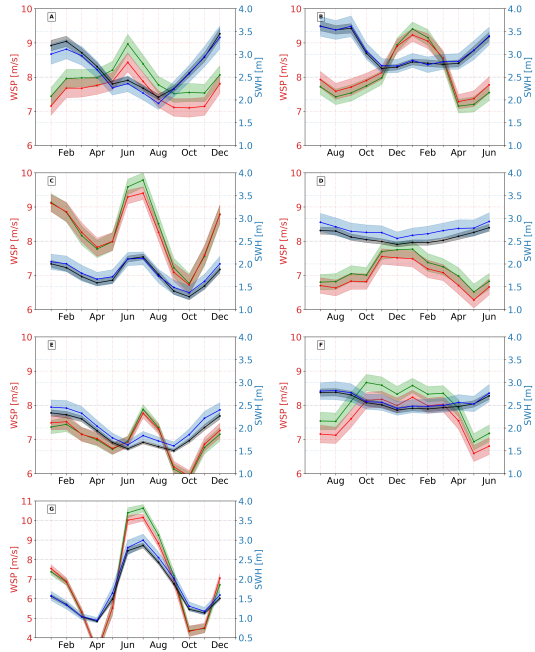
588 By computing probability of swell globally for each season using wave age, prob-
 589 ability of swell in SWA regions can confirm if the wave field observed during the spring
 590 months in SWA regions were dominated by wind-seas generated by the local wind anomaly
 591 or dominated by swell propagating from distant storms.

592 To calculate phase speed of waves and therefore wave age, we used Wave Watch
 593 3 (WW3) modeled data with peak frequency. The Climate Forecast System Reanaly-
 594 sis (CFSR) winds provided the forcing to WW3 wave model in order to obtain the bulk
 595 parameters SWH and peak frequency with 6 hourly temporal and 0.5 degree spatial res-
 596 olution. Wave age was computed after decreasing the spatial resolution of WW3 peak
 597 frequency and CFSR WSP to 1 degree and the temporal resolution to daily time steps.
 598 The WW3 and CFSR products were used instead of the coupled ECMWF wind prod-
 599 uct and WW3 wave parameters because CFSR WSP forcing WW3 SWH has more sea-
 600 sonal variability, and prediction accuracy improves in recent years (Stopa & Cheung, 2014a).
 601 However, the WW3 and CFSR data sets has some potential biases, including overesti-
 602 mation of SWH and WSP as compared to in situ buoy observations and less temporal

homogeneity than ECMWF forcing WW3 model which manifests itself as a slightly less smooth time series allowing CFSR and WW3 to more accurately model extreme weather events (Stopa & Cheung, 2014a).

Before computing wave age with WW3 peak frequency using CFSR winds, we performed an elementary comparison test between remotely sensed SWH and WSP observations and WW3 SWH and CFSR WSP to understand how well the WW3 SWH and CFSR WSP were representing the observational data. This validation process included computing regional climatologies of WW3 SWH and CFSR WSP data in the same regions which that observational SWH and WSP climatologies were computed. In addition, the least-squares fit annual and semi-annual model was fitted to WW3 SWH and CFSR WSP and parameters of model were computed. Before performing comparison, the WW3 and CFSR data resolutions were decreased spatially to 1° by 1° and temporally to monthly time steps in order to match the data resolution of the least squares fit and regional climatology analysis. This prevents the model's small-scale spatial variability from artificially reducing correlations between the modelled and observed data. Regional climatologies of WW3 SWH and CFSR WSP data are compared to the Ifremer SWH and CCMP2 WSP in Fig 12, and the parameters of the least-squares fit of WW3 SWH and WSP (not shown). Both regional climatologies and parameters of the 5 parameter least square fit show high agreement in all of the SWA regions. This means that the amplitude and phase of the annual and semi-annual cycles agree well in SWA regions. However, there are small disparities present. For the regional climatologies, the model underestimates or agrees well with SWH in all SWA region climatologies except off the California coast where the model consistently overestimates (Fig 12). The model overestimates WSP off the coasts of California, Chile, and Namibia (Fig 12A,D,F). In SWA regions off the coast of west Australia, north Africa, south Caribbean, and the Arabian Sea, the model overestimates the climatological maxima while underestimating the minima.

What are the consequences of overestimating or underestimating WSP on the probability of swell if assuming peak frequency is unbiased and is held constant? By overestimating WSP, wave age would decrease (increasing the denominator and decreases wave-age ratio) making it more likely for wave age drop below 1.2 and the wave field to be categorized as wind-sea dominated. This would lead to a decrease the probability of swell. Therefore, there may be a bias toward low probability of swell in SWA regions including Northern California, Chile, and Namibia. Using the same rational as before, for the southern Caribbean and Arabian Seas, there is a bias toward lower probability of swell during the boreal summer when the local wind anomaly occurs due to CFSR overestimates WSP. For northern Africa, the probability of swell would have very little bias introduced by the WSP data due to the high accuracy of the model. For Western Australia, there is a slight bias toward lower probability of swell in the austral summer and higher probability of swell in the austral winter due to the CFSR underestimating WSP. Next, peak frequency must be validated by comparing it with in situ observations. Performance assessments of WW3 peak frequency have been studied in the Pacific basin by Hanson, Tracy, Tolman, and Scott (2009) using the Wave Model Evaluation and Diagnostics System (WaveMEDS) to quantify the biases and overall performance scores for peak period for the entire wave field and for each component (wind-seas and swell) for the year 2000. The WW3 wave model had wind forcing from the high-quality, consistent, neutral stability wind fields NRAQ+ generated by the marine meteorology group at Oceanweather Inc. (Hanson et al., 2009). This is not the same wind forcing used to force the WW3 peak frequency data in this study, however, Hanson et al. (2009) has validated the peak frequency with realistic and reliable wind forcing. The WW3 modeled wave spectra is compared with wave spectra from seven deep-water buoy sites from the National Data Buoy Center (NDBC) and the Coastal Data Information Program (CDIP). Hanson et al. (2009) concluded that wave period agrees with in situ observations with



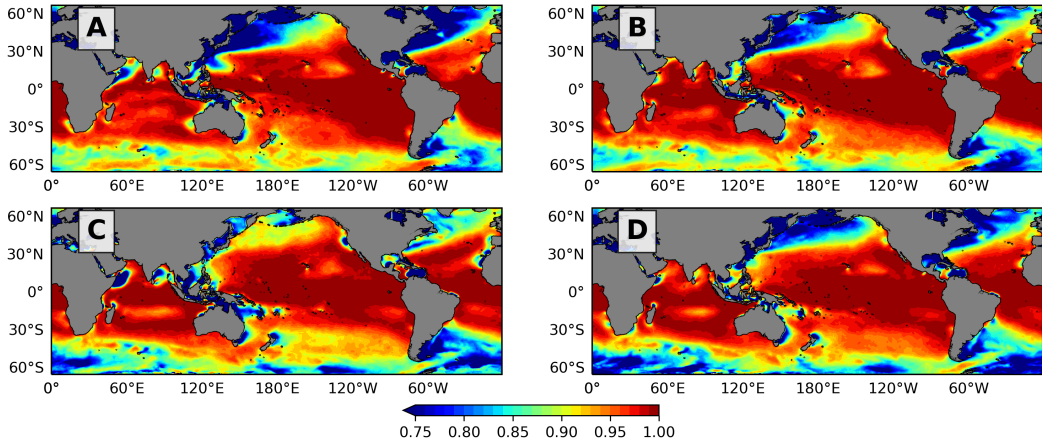
663 **Figure 12.** Northern Hemisphere SWA regions: (A) North California, (C) Southern
 664 Caribbean, (E) North Africa, and (G) Arabian Sea which are the same regions as in Fig 9 and
 665 Southern Hemisphere SWA regions: (B) West Australia, (D) coast of Chile, and (F) coast of
 666 Namibia which are the same regions as in Fig 10

666 a combined wind-sea and swell waves performance score of 0.93 for temporal correlations
 667 and 0.96 for quantile-quantile (Hanson et al., 2009).

668 The validation of the wave parameter peak frequency occurs with buoys located
 669 primarily in the Northern Hemisphere pacific. Other ocean basins have still yet to be
 670 rigorously validated for peak frequency. With the fore knowledge that the performance
 671 of peak frequency is unknown in other ocean basins, we use peak frequency based on the
 672 high accuracy of the model in representing in situ observations in the pacific.

673 Figure 13 is a seasonal progression global map of probability of swell which agrees
 674 very well with Semedo et al. (2011) global maps of probability of swell for DJF and JJA.
 675 As observed in Figure 13, SWA regions contained waves that were categorized as locally
 676 forced during the late spring and early summer months. This is illustrated by the prob-
 677 ability of swell being significantly lower in SWA regions than the surrounding areas around
 678 SWA regions during the season when the wind anomaly occurs. For the northern hemi-
 679 sphere, off the coast of California, the probability of swell significantly drops to 90% in
 680 the spring months and then below 75% in the summer months. Similarly, off the coast
 681 of North Africa, probability of swell drops to between 90% to 80% in the spring months
 682 and then below 75% in the summer months. Both the Caribbean and Arabian Seas are
 683 consistently below 75% through the entire year. This means that the wave field is more
 684 frequently dominated by locally forced waves than remotely forced waves. Therefore, this
 685 result agrees with the hypothesis that the deviation from the SWH annual cycle is a re-
 686 sult from locally forced waves dominating the wave field and causing a increase in SWH.
 687 For the Southern Hemisphere, the probability of swell in the SWA regions of West Aus-
 688 tralia, Chile, and Namibia is not as low as in other SWA regions. This would also agree
 689 with the hypothesis that the SWA regions in the Southern Hemisphere have wave fields
 690 that are dominated predominately by remotely forced waves (and dominated by locally

685 forced wave on fewer occurrences) due to their proximity to the Southern Ocean lead-
 686 ing to a less pronounced or nonexistent deviation from the SWH annual cycle.



687 **Figure 13.** Seasonal progression of probability of swell using wave age criterion and WW3
 688 peak frequency and WSP from January 1st, 1993 to December 31st, 2015 where (A) DJF, (B)
 689 MAM, (C) JJA, and (D) SON

690 5 Conclusion

691 This study has analyzed the seasonal cycles of SWH and WSP by least-squares fit-
 692 ting annual and semi-annual cycles to satellite observations. In most of the ocean, SWH
 693 is higher in winter, indicating a response to high-latitude winter storms that generate
 694 equatorward-propagating swell. Exceptions occur in a few eastern boundary current re-
 695 gions and other wind anomaly regions, where strong local winds in spring or summer gen-
 696 erate wind waves that are out of phase with the winter storms. In the equatorial region,
 697 the boundary where the domains of dominance of Northern and Southern Hemisphere
 698 storm patterns setting the SWH annual cycle occurs off the equator in the Southern Hemis-
 699 phere following the line where the amplitude of the SWH annual cycle vanishes. This
 700 boundary is hypothesized to be influenced significantly by Polynesian islands affecting
 701 the way waves propagate through this region. Using regional climatology analysis in 4°
 702 by 4° boxes, we find that in SWA regions, the SWH can deviate from a sinusoidal an-
 703 nual cycle with winter maximum, instead indicating direct response to local winds. In
 704 SWA regions, the fraction of wave variability attributed to local wind events varies de-
 705 pending on local conditions. 16.4% of the world oceans including all but one of the SWA
 706 regions experience an anomalous WSP seasonal variability with the maximum of the WSP
 707 seasonal cycle occurring outside of the winter months of the respective hemisphere. The
 708 waves within each SWA region have low probability of swell during the spring and sum-
 709 mer months of each hemisphere respectively. This implies that there is an increase in the
 710 number of times the wave field is dominated by wind-seas, supporting the hypothesis that
 711 the deviation from the SWH annual cycle results from wave that are locally forced by
 712 a local wind events.

713 Further research would include using spectral data from WW3 waves model forced
 714 by CFSR winds in order to separate wind-sea and swell parameters in SWA regions via
 715 spectral partitioning (Portilla et al., 2009) to further validate the claim that the devi-
 716 ation in the SWH seasonal cycle occurs from local wind events. In addition, local wind

717 events should be further investigated to evaluate whether local winds result from the same
 718 atmospheric coastal topographic processes as in California.

719 By improving our understanding of the SWH climate globally with respect to the
 720 effects of local wind events, wave models can more accurately model and anticipate in-
 721 creases in SWH. Through understanding the wave climate in these SWA regions, we gain
 722 greater insight into determining at what times during the year remotely and locally forced
 723 wind waves dominate the wave field. Wave field's dominated by locally forced waves have
 724 strong interactions between waves and the lowest atmospheric layer (Cavaleri et al., 2012)
 725 due to the tendency of waves have short frequencies and steep. Processes involved in air-
 726 sea interactions that are amplifies by locally forced waves includes wave breaking and
 727 white capping. Both of these processes leads increase heat and mass fluxes from eject-
 728 ing sea spray including aerosols into the atmospheric boundary layer, injecting bubbles
 729 into the ocean, and causing waving-induced mixing in the upper ocean layer (Cavaleri
 730 et al., 2012). Sea-state dependent surface wave modulated fluxes of momentum, energy,
 731 heat and mass are all essential for climate models being able to close budgets to full de-
 732 scribe the coupled ocean-atmosphere system (Cavaleri et al., 2012). Understanding these
 733 fluxes begins with knowing the large scale temporally and spatially tendencies of the sea-
 734 state of the ocean. Through this study, identification of regions with high tendency for
 735 wind-sea dominated wave fields during the spring and summer months are established.
 736 From here, we can hypothesize general expectations for the significant air-interaction pro-
 737 cesses present in these regions.

738 Acknowledgments

739 This work was supported by NASA SWOT and Ocean Vector Winds Science Teams, Ana
 740 Villas Bôas Nasa fellowship, and the Hiestand Scholars program. The authors acknowl-
 741 edge Remote Sensing Systems for providing the multi-platform wind speed data avail-
 742 able from www.remss.com (<ftp://ftp.remss.com/ccmp/v02.0>) and the *French Research
 743 Institute for Exploitation of the Sea* (IFREMER) for providing the satellite altimetry sig-
 744 nificant wave height data (<ftp://ftp.ifremer.fr/ifremer/cersat/products/swath/altimeters/waves>)
 745 and WaveWatch 3 hindcast (<ftp://ftp.ifremer.fr/ifremer/ww3/HINDCAST>).

746 References

- 747 Alves, J. H. G., Banner, M. L., & Young, I. R. (2003). Revisiting the pierson-
 748 moskowitz asymptotic limits for fully developed wind waves. *Journal of physi-
 749 cal oceanography*, 33(7), 1301–1323.
- 750 Arduin, F. (2018). *Ocean waves in geosciences*. doi: 10.13140/RG.2.2.16019.78888/
 751 5
- 752 Arduin, F., Chapron, B., & Collard, F. (2009). Observation of swell dissipation
 753 across oceans. *Geophysical Research Letters*, 36(6).
- 754 Atlas, R., Hoffman, R. N., Ardizzone, J., Leidner, S. M., Jusem, J. C., Smith, D. K.,
 755 & Gombos, D. (2011). A cross-calibrated, multiplatform ocean surface wind
 756 velocity product for meteorological and oceanographic applications. *Bull.
 757 Amer. Meteor. Soc.*, 92, 157-174. doi: 10.1175/2010BAMS2946.1
- 758 Boas, A. B. V., Arduin, F., Ayet, A., Bourassa, M. A., Brandt, P., Chapron, B., ...
 759 others (2019). Integrated observations of global surface winds, currents, and
 760 waves: Requirements and challenges for the next decade. *Frontiers in Marine
 761 Science*, 6.
- 762 Cavaleri, L., Fox-Kemper, B., & Hemer, M. (2012). Wind waves in the coupled cli-
 763 mate system. *Bulletin of the American Meteorological Society*, 93(11), 1651–
 764 1661.
- 765 Chelton, D. B., Ries, J. C., Haines, B. J., Fu, L.-L., & Callahan, P. S. (2001). Satel-
 766 lite altimetry. In *International geophysics* (Vol. 69, pp. 1–ii). Elsevier.
- 767 Chen, G., Chapron, B., Ezraty, R., & Vandemark, D. (2002). A global view of swell

- and wind sea climate in the ocean by satellite altimeter and scatterometer. *Journal of Atmospheric and Oceanic Technology*, 19(11), 1849–1859.
- Croiz-Fillon, P. Q. . D. (2017). *Global altimeter swh data set* (Vol. 2; Tech. Rep.). ZI de la pointe du diable, CS10070, 29280 Plouzan, France.
- Donelan, M., Skafel, M., Graber, H., Liu, P., Schwab, D., & Venkatesh, S. (1992). On the growth rate of wind-generated waves. *Atmosphere-Ocean*, 30(3), 457–478.
- Echevarria, E., Hemer, M., & Holbrook, N. (2019). Seasonal variability of the global spectral wind wave climate. *Journal of Geophysical Research: Oceans*, 124(4), 2924–2939.
- Edson, J., Crawford, T., Crescenti, J., Farrar, T., Frew, N., Gerbi, G., ... others (2007). The coupled boundary layers and air-sea transfer experiment in low winds. *Bulletin of the American Meteorological Society*, 88(3), 341–356.
- Hanson, J. L., Tracy, B. A., Tolman, H. L., & Scott, R. D. (2009). Pacific hind-cast performance of three numerical wave models. *Journal of Atmospheric and Oceanic Technology*, 26(8), 1614–1633.
- Jiang, H., & Chen, G. (2013). A global view on the swell and wind sea climate by the jason-1 mission: a revisit. *Journal of Atmospheric and Oceanic Technology*, 30(8), 1833–1841.
- Munk, W. H. (1951). *Origin and generation of waves* (Tech. Rep.). SCRIPPS INSTITUTION OF OCEANOGRAPHY LA JOLLA CALIF.
- Portilla, J., Ocampo-Torres, F. J., & Monbaliu, J. (2009). Spectral partitioning and identification of wind sea and swell. *Journal of atmospheric and oceanic technology*, 26(1), 107–122.
- Queffeulou, P. (2004). Long-term validation of wave height measurements from altimeters. *Marine Geodesy*, 27(3-4), 495–510.
- Schneider, T., Bischoff, T., & Haug, G. H. (2014). Migrations and dynamics of the intertropical convergence zone. *Nature*, 513(7516), 45.
- Schott, F. A., Xie, S.-P., & McCreary Jr, J. P. (2009). Indian ocean circulation and climate variability. *Reviews of Geophysics*, 47(1).
- Semedo, A., Sušelj, K., Rutgersson, A., & Sterl, A. (2011). A global view on the wind sea and swell climate and variability from era-40. *Journal of Climate*, 24(5), 1461–1479.
- Snodgrass, F., Hasselmann, K., Miller, G., Munk, W. H., & Powers, W. (1966). Propagation of ocean swell across the pacific. *Philosophical Transactions of the Royal Society of London. Series A, Mathematical and Physical Sciences*, 259(1103), 431–497.
- Stopa, J. E. (2019). Seasonality of wind speeds and wave heights from 30 years of satellite altimetry. *Advances in Space Research*.
- Stopa, J. E., & Cheung, K. F. (2014a). Intercomparison of wind and wave data from the ecmwf reanalysis interim and the ncep climate forecast system reanalysis. *Ocean Modelling*, 75, 65–83.
- Stopa, J. E., & Cheung, K. F. (2014b). Periodicity and patterns of ocean wind and wave climate. *Journal of Geophysical Research: Oceans*, 119(8), 5563–5584.
- Sullivan, P. P., McWILLIAMS, J. C., & Melville, W. K. (2004). The oceanic boundary layer driven by wave breaking with stochastic variability. part 1. direct numerical simulations. *Journal of Fluid Mechanics*, 507, 143–174.
- Sverdrup, H. U., & Munk, W. H. (1947). *Wind, sea and swell: Theory of relations for forecasting* (No. 303). Hydrographic Office.
- Talley, L. D. (2011). *Descriptive physical oceanography: an introduction*. Academic press.
- Villas Bôas, A. B., Gille, S. T., Mazloff, M. R., & Cornuelle, B. D. (2017). Characterization of the deep water surface wave variability in the california current region. *Journal of Geophysical Research: Oceans*, 122(11), 8753–8769.
- Winant, C., Dorman, C., Friehe, C., & Beardsley, R. (1988). The marine layer off

- 823 northern california: An example of supercritical channel flow. *Journal of the*
824 *Atmospheric Sciences*, 45(23), 3588–3605.
- 825 Young, I. (1999). Seasonal variability of the global ocean wind and wave climate.
826 *International Journal of Climatology: A Journal of the Royal Meteorological*
827 *Society*, 19(9), 931–950.
- 828 Young, I., Zieger, S., & Babanin, A. V. (2011). Global trends in wind speed and
829 wave height. *Science*, 332(6028), 451–455.
- 830 Zheng, K., Sun, J., Guan, C., & Shao, W. (2016). Analysis of the global swell and
831 wind sea energy distribution using wavewatch iii. *Advances in Meteorology*,
832 2016.